Proceedings of IJTC2006
STLE/ASME International Joint Tribology Conference
October 22-25, 2006, San Antonio, TX, USA

IJTC2006-12103

MODELING OF THE ROLLING AND SLIDING CONTACT BETWEEN TWO ASPERITIES

PART I: NUMERICAL METHODOLOGY

V. Boucly (LaMCoS – UMR CNRS 5514, INSA Lyon, France)

D. Nélias (LaMCoS – UMR CNRS 5514, INSA Lyon, France)

I. Green (Georgia Institute of Technology, Atlanta, USA)

ABSTRACT

A semi-analytical method for the tridimensional thermal-elastic-plastic contact between two hemispherical asperities is proposed. This first part of the paper describes the algorithm used to deal with the normal contact, which can be either load-driven (ld) or displacement-driven (dd). Both formulations use the Conjugate Gradient (CG) method and the Discrete Convolution and Fast Fourier Transform (DC-FFT) technique. A validation of the code is made in the case of the displacement-driven formulation for an elastic-plastic body in contact with a rigid punch, simulating a nano-indentation test. For both formulations (ld and dd) a very good convergence rate is found. Another new feature is the treatment of the contact between two elastic-plastic bodies. The model is first validated through comparison with the Finite Element Method (FEM). The contact pressure distribution, the hydrostatic pressure and the equivalent plastic strain state below the contacting surfaces are also found to be strongly modified in comparison to the case of an elastic-plastic body in contact with a purely elastic body. An application to the tugging between two spherical asperities in simple sliding (dd formulation) is made in part II of the paper.

INTRODUCTION

It is now well recognized that Semi-Analytical Methods (SAM) are efficient methods for solving contact problems. Compared to Finite Element (FE) analyses, SAM show much shorter computation times, typically by several orders of magnitude. Among many numerical methods it seems that the most efficient to solve contact problem are the Conjugate Gradient (CG) method first introduced by Nogi and Kato [1], later used by Polonsky and Keer [2], the Multi Level Multi Summation (MLMS) technique first implemented by Lubrecht and Ioannides [3], and the Discrete Convolution and Fast Fourier Transform (DC-FFT) used by Nogi and Kato [1] and later by Liu et al. [4] combined to the CGM. The present paper is in the continuity of the work by Nélias and co-workers [5-11] who developed a semi-analytical method for solving contact problems with different levels of complexity ranging from elastic-plastic (EP) rolling contact simulation [5], thermal-elastic-plastic (TEP) analysis [6], normally and tangentially loaded EP contact [7] with various potential applications such as the determination of the micro-yield stress profile in a nitrided steel by nano-indentation [8], the rolling of a load on a smooth, dented or rough surface [5, 9], the simulation of fretting wear [10], and the running-in or wear of initially smooth or rough surfaces [11].

NOMENCLATURE

Elastic contact resolution (CGM)

u = elastic displacement, m
p = pressure, Pa
h = surface separation, m
α = interference, m
g = gap, m
P_0 = initial load, N
P = load, N
S_g = grid area
I_g = set of nodes in the grid
I_c = set of grid nodes in contact
I_{ol} = set of grid nodes where there is no contact and where the surfaces overlap
t = direction of the gradient
r = residue
τ = step length

(Thermal-)Elastic-Plastic contact resolution

u^e = elastic displacement, m
u^t = thermal displacement, m
u^r = residual displacement, m

h^0 = initial surface separation, m
ε^p = plastic strain tensor, -
e^p = equivalent plastic strain, -
σ^r_1, σ^r_2, σ^r_3 = principal components of the residual stress tensor
P^L = interpolation polynom
P_j^L = Lagrange polynoms
C(%) = percentage difference between E_EP and EP_EP max pressures
L_c = critical load for 0.2% equivalent plastic strain, N

Elastic constants
ν = Poisson ration
E = Young modulus, Pa
E' = equivalent Young modulus, Pa

Geometry
R_1 , R_2 = radius of body 1 and 2, respectively, m
R = equivalent radius, m

LOAD-DRIVEN (LD) VS. DISPLACEMENT-DRIVEN (DD) FORMULATIONS

In order to simulate the rolling/sliding contact, a ld formulation was first used by applying a normal load (vertical loading) prior to the tangential displacement of the load (rolling load). In such a formulation one may consider a frictionless contact, see for example [5, 6, 9], as well as the effect of friction which often tends to overload the near surface area [7, 11]. This formulation is well adapted when considering the whole contact between two bodies pressed against each other with a prescribed load. On the other hand, when focusing the analysis to the contact between two single asperities led on opposite surfaces which are in relative motion, it is clear that this localized interaction is more related to a rigid body displacement (interference) producing a transient normal and tangential loading when asperities collide. It should be noted that the tangential load is here defined as the force that acts opposite to the relative velocity, which is not limited to frictional effects since the contact surface is barely parallel to the relative velocity between the contacting surfaces. This is the reason why a friction coefficient is purposely omitted in this study, in order to uncouple tangential effects induced by mechanical deformations, and the ones induced by friction. The mechanism at the origin of the tangential load found when two asperities tug each other is similar to the one found during ploughing when a normally loaded rigid indenter is translated on the surface of a deformable media.

A realistic application of the sliding between two asperities with a fixed value of the interference could be the sliding of a projectile between two rails in an electromagnetic launcher for example, since the projectile is sliding on two rails that are fixed in distance.

The model is based on the work of Polonsky and Keer [2] that developed a load driven formulation for the normal contact. In their formulation, they used the CG method and the MLMS technique to accelerate the computation speed. Based on the same formulation but using a different numerical procedure, i.e. using the DC-FFT technique instead of the MLMS technique, Liu et al. [12] found a better convergence rate and improved accuracy [4].

Basically the load driven formulation shows very good results in terms of convergence rate and accuracy, but the user is forced to fix a value for the load, resulting in finding a rigid body displacement after computation. As said earlier, this is convenient for the resolution of the whole contact, but not to describe the tugging between two single asperities. Thereafter are presented the contact algorithms first for the load driven formulation and second for the displacement driven formulation.

Elastic contact problem

The pressure distribution in the contact conjunction creates a composite displacement *u(x,y)*, which is the summation of the two displacements on the surface of each body at the point of coordinate *(x,y)*, given by:

$$u(x,y) = -\iint_{S_g} K(x-x', y-y')\,p(x',y')\,dx'dy' \qquad (1)$$

In this expression, S_g is the grid area and $K(x, y)$ stands for the surface deflection distribution produced by a concentrated normal contact load of unit magnitude acting at the origin of the domain. For a pair of homogeneous elastic solids in contact, the kernel $K(x,y)$ is given by the Boussinesq formula [13]:

$$K(x,y) = \left(\frac{1-\nu_1^2}{\pi E_1} + \frac{1-\nu_2^2}{\pi E_2}\right)\frac{1}{\sqrt{x^2+y^2}} \qquad (2)$$

where E_1 and E_2 are the Young moduli of the two solids, and ν_1 and ν_2 are their Poisson's ratios. The grid area S_g is divided into N rectangular surface elements S_{ij} centered at the grid nodes. The length and the width of each element are equal to the grid spacings in the x and y-directions, respectively. The contact pressure distribution is approximated by a piecewise constant function, uniform within each surface element. Denoting I_g the set of all nodes in the grid, Eq. 1 can be re-written as:

$$u_{ij} = -\sum_{(k,l)\in I_g} K_{i-k,\,j-l}\,p_{kl}\,, \quad (i,j)\in I_g \qquad (3)$$

where u_{ij} is the surface deflection at node (i, j), p_{kl} is the uniform pressure acting on the element centered at node (k,l), and K_{ij} are the influence coefficients, given by:

$$K_{ij} = \iint_{S_{00}} K(x_i - x', y_j - y')\,dx'dy', \quad (i,j)\in I_g \qquad (4)$$

In the case of homogenous elastic solids, the coefficients K_{ij} can be easily calculated using the well-known closed-form solution for a patch load acting on an elastic half-space [13]. The calculation of the elastic displacement in Eq. 3 is done using the DC-FFT method, as introduced by Liu [4].

Taking into account the expression of the elastic displacement in Eq. 3, the contact problem can be described by the following system of equations and inequalities:

$$\sum_{(k,l)\in I_g} K_{i-k,j-l}\, p_{kl} = h_{ij} + \alpha, \quad (i,j)\in I_c \tag{5a}$$

$$p_{ij} > 0, \quad (i,j)\in I_c; \tag{5b}$$

$$\sum_{(k,l)\in I_g} K_{i-k,j-l}\, p_{kl} \ge h_{ij} + \alpha, \quad (i,j)\notin I_c; \tag{5c}$$

$$p_{ij} = 0, \quad (i,j)\notin I_c; \tag{5d}$$

$$a_x a_y \sum_{(i,j)\in I_g} p_{ij} = P_0. \tag{5e}$$

where α is the rigid body approach (interference) between the two solids, a_x and a_y are the grid spacings in x and y directions respectively, P_0 is the total normal load, h_{ij} is the total separation between the two solids and I_c denotes the set of all grid nodes that are in contact. In the case of the displacement driven contact problem, the load is unknown, then Eq. 5e is not valid any longer. Since one equation has been removed, one unknown – the interference α – should also be removed from the set of unknowns in the numerical procedure.

Solving the elastic contact using CGM and DC-FFT

Hereafter the elastic contact algorithm used for both ld and dd formulations is briefly presented. Differences in the algorithm due to the formulation chosen are outlined. For a more complete description of the algorithm and the assumptions, the reader may refer to [2].

At first, an initial value of the pressure must be fixed and Eqs. 5b, 5d and 5e have to be verified. In order to verify Eqs. 5b and 5d it is required to choose non-negative values for the discrete pressure. For Eq. 5e, for simplicity, each point of the surface is assigned a value of the pressure corresponding to the total load divided by the surface area, i.e. the number of grid points multiplied by the elementary surface area $dS = a_x \times a_y$. It is to be noticed, though, that the pressure distribution can be taken arbitrarily as long as it obeys Eq. 5e.

For the displacement driven formulation, the load is unknown, but could be estimated at the initial state by using the Hertz theory, see for example [14]:

$$P_0 = \frac{4}{3} E' \sqrt{R}\,(\alpha)^{3/2} \tag{6}$$

In this expression, R is the equivalent radius given in Eq. 7 and E' is the equivalent Young modulus given by Eq. 8.

$$\frac{1}{R} = \frac{1}{R_1} + \frac{1}{R_2} \tag{7}$$

$$\frac{1}{E'} = \frac{1-\nu_1^2}{E_1} + \frac{1-\nu_2^2}{E_2} \tag{8}$$

Two other variables are introduced, δ and G_{old} that are initialized by setting $\delta=0$ and $G_{old} = 1$.

The displacements u_{ij} are then computed and the iteration can start. The first step is the calculation of the gap g. For the load driven formulation, it gives:

$$g_{ij} = -u_{ij} - h_{ij}, \quad (i,j)\in I_g; \tag{9}$$

$$\bar{g} = N_c^{-1} \sum_{(k,l)\in I_c} g_{kl}; \tag{10}$$

$$g_{ij} \leftarrow g_{ij} - \bar{g}, \quad (i,j)\in I_g. \tag{11}$$

where N_c is the number of points in the contact area, which means all the grid points where the pressure is not nil but positive.

For the displacement driven formulation, the calculation of the gap g gives:

$$g_{ij} = -u_{ij} - h_{ij} - \alpha, \quad (i,j)\in I_g \tag{12}$$

Once g_{ij} is calculated, G is computed as follow:

$$G = \sum_{(i,j)\in I_c} g_{ij}^2 \tag{13}$$

$$G_{old} = G \tag{14}$$

G and G_{old} are used for the calculation of the new conjugate direction t_{ij}:

$$t_{ij} \leftarrow g_{ij} + \delta\left(G/G_{old}\right) t_{ij}, \quad (i,j)\in I_c; \tag{15}$$

$$t_{ij} = 0, \quad (i,j)\notin I_c. \tag{16}$$

In order to calculate the length of the step that will be made in the direction t_{ij}, r_{ij} is calculated as follow:

$$r_{ij} = \sum_{(k,l)\in I_g} K_{i-k,j-l}\, t_{kl}, \quad (i,j)\in I_g \tag{17}$$

Since Eq. 17 is a convolution product, the calculation of the r_{ij} is done using the DC-FFT method [4], the same way as the elastic displacements were calculated in Eq. 3.

For the load-driven formulation, the residual r_{ij} is adjusted to deal with the interference calculation enforcement:

$$\bar{r} = N_c^{-1} \sum_{(k,l)\in I_c} r_{kl}; \tag{18}$$

$$r_{ij} \leftarrow r_{ij} - \bar{r}, \quad (i,j)\in I_g. \tag{19}$$

This step is not required for the displacement driven formulation since the interference is known.

The length of the step τ can now be calculated, giving for both formulations:

$$\tau = \frac{\sum_{(i,j)\in I_c} g_{ij} t_{ij}}{\sum_{(i,j)\in I_c} r_{ij} t_{ij}} \tag{20}$$

Before updating the pressure, the current pressure value is stored for the error calculation:

$$p_{ij}^{old} = p_{ij}, \quad (i,j)\in I_g \tag{21}$$

The new pressure distribution is then calculated using the previous calculated step and direction:

$$p_{ij} \leftarrow p_{ij} - \tau\, t_{ij}, \quad (i,j) \in I_c \tag{22}$$

After this step, Eq. 5d must be verified. Then, for all the grid nodes where the pressure is found negative, a nil value is enforced:

$$if \quad p_{ij} < 0 \quad then \quad p_{ij} = 0 \tag{23}$$

Denoting I_{ol} the set of nodes where there is no contact and where the surfaces overlap, i.e.

$$I_{ol} = \{(i,j) \in I_g : \quad p_{ij} = 0,\, g_{ij} < 0\} \tag{24}$$

then δ set equal to unity if $I_{ol} = \emptyset$. Otherwise, δ is set to zero and the pressures are corrected where the surfaces overlap:

$$p_{ij} \leftarrow p_{ij} - \tau\, g_{ij}, \quad (i,j) \in I_{ol} \tag{25}$$

In the case of the load-driven formulation, Eq. 5e is still to be verified. To do so, the force balance condition is enforced, and the pressures are corrected as follow:

$$P = a_x a_y \sum_{(i,j)\in I_g} p_{ij}; \tag{26}$$

$$p_{ij} \leftarrow (P/P_0)\, p_{ij}, \quad (i,j) \in I_g \tag{27}$$

This step is not required for the displacement driven formulation, since Eq. 5e is not part of the problem.

Finally the error is computed as follow:

$$\varepsilon = a_x a_y P^{-1} \sum_{(i,j)\in I_g} \left| p_{ij} - p_{ij}^{old} \right| \tag{28}$$

and a new iteration is performed, unless convergence is reached, i.e. $\varepsilon \le \varepsilon_0$, with ε_0 the prescribed error.

Application to the thermal-elastic-plastic formulation

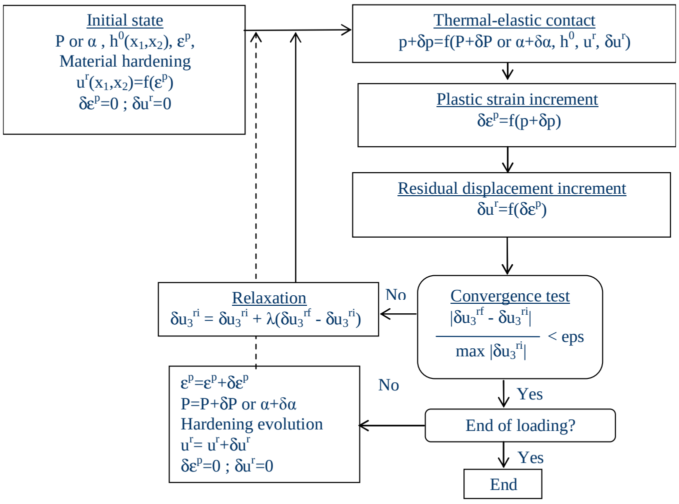

Fig. 1 – Thermal-elastic-plastic algorithm

The elastic contact solver is one part of the (thermal)-elastic-plastic contact code. For a complete description of the problem, the reader is referred to both [5] and [6]. A return-mapping algorithm with an elastic predictor/plastic corrector scheme and a von Mises criterion has also been implemented, improving the plasticity loop, see [11]. This improvement in the numerical algorithm increases the computing speed significantly and shows a much better convergence and accuracy. An overview of the algorithm is given in Fig 1.

Starting from an initial state which is the application of a load P or an interference α, any initial geometry, some plastic strains and a hardening state, a first residual displacement is calculated, see [5, 6] for calculation details. The plastic strain increment $\delta\varepsilon^p$ and the residual displacement increment δu^r are initially set to zero. The thermal-elastic contact is then calculated using the method proposed in the previous section, but replacing u_{ij} by the displacement calculated in Eq. 29 and replacing h_{ij} by the updated geometry calculated in Eq. 30, which takes into account the residual displacement found at the previous step of the iteration process.

For a more detailed description, the reader is referred to [6].

$$u_{ij} = u_{ij}^e + u_{ij}^t \tag{29}$$

with u_{ij} the total displacement, u^e_{ij} the elastic displacement as expressed in Eq. 1, and u^t_{ij} the thermally induced displacement [12].

$$\mathrm{h}_{ij} \leftarrow \mathrm{h}_{ij} + \mathrm{u}_{ij}^{r} \tag{30}$$

with h_{ij} the updated geometry, and u^r_{ij} the residual displacement.

Then, the plastic strain increment $\delta\varepsilon^p$ is computed, using a return mapping scheme, based on the Newton Raphson method. The algorithm used is presented by Fotiu and Nemat-Nasser in [15], and applied to the current model in [11].

The next step is the calculation of the residual displacement increment [5] which is added to the initial geometry in Eq. 30 until convergence is reached. At this point, for a vertical loading, either the load P or the interference α is increased by an increment, and the iteration procedure is carried on. For rolling loading in the ld formulation, the load is kept constant whereas the hardening state and the plastic strains are updated after each increment. For rolling / sliding loading in the dd formulation, the interference, the hardening state and the plastic strains are updated before the next step of the iteration process.

Validation of the dd-driven algorithm

In the case of the contact between an elastic-plastic body and a rigid punch (nano-indentation test), the load-driven formulation has been validated with the Finite Element software Abaqus, and also experimentally, see [5]. For this simulation, the elastic-plastic body is a flat made of steel used in aeronautic applications. The elastic properties of this steel are E=210GPa for the Young modulus, and ν=0.3 for Poisson ratio. The Swift law is used to describe the hardening behavior, see Eq. 31 and the chosen parameters are B=1240MPa, C=30, and n=0.085. It is to be noted that the equivalent plastic strain in this expression is expressed in microdef (10^{-6} def). These values are taken according to El Ghazal [16] and correspond to the experimental data presented in [5].

$$\sigma_{VM} = B \cdot \left(C + e^{p}\right)^{n} \qquad (31)$$

For the rigid punch, a sphere with radius 105 µm is chosen (nano-indenter tip). The load is progressively applied until 0.650 N and then the two bodies are unloaded until no contact occurs anymore.

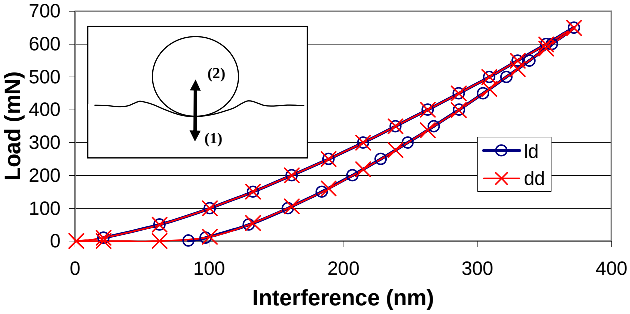

Fig. 2 – Load (mN) vs. interference during the loading / unloading phases. Max load 0.650 N / Max interference 372 nm

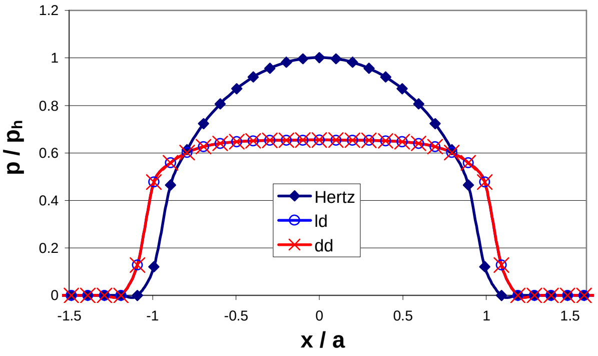

Fig. 3 – Pressure distribution at the end of the loading phase, in the plane y=0. Load 0.650 N

Figures 2 and 3 present a comparison between the load-driven and the displacement-driven formulations.

Figure 2 gives the evolution of the load versus the interference during loading and unloading. It is observed here the influence of both plasticity and conformity change due to permanent deformation of the surface, since the curves are really different for the loading and the unloading phases. Plasticity is a phenomenon that depends on the loading history.

The pressure distribution in the plane y=0 (longitudinal plane) for the maximum load of 0.650 N at the end of the loading phase, is given in Fig. 3. The pressure distribution is found flattened compared to the Hertz solution. This is due mostly to hardening of the elastic-plastic material which tends to increase the contact area. There is also a little influence of the geometry change due to permanent deformation of the surface.

As it can be seen, a very good agreement is found, for a comparable time computation with for the mesh-size, dx=0.6µm, dy=1.2µm, dz=0.3µm i.e. 31 x 17 x 44 = 23,188 points in the plastic zone and with a total of 26 time-step increments for loading / unloading (about 25 minutes for the whole loading / unloading process on a 1.8 GHz Pentium M personal computer).

MODELING OF THE CONTACT BETWEEN TWO ELASTIC-PLASTIC BODIES

This paragraph deals with the contact between two elastic-plastic bodies. The current assumptions are that the two bodies have the same initial geometry with identical elastic properties and hardening behavior. In order to validate the new proposed algorithm, a comparison with a Finite Element simulation is made through the normal contact between two spheres. The differences between the case of an elastic plastic body in contact with another elastic plastic body, and the case of an elastic plastic body in contact with a pure elastic body will be outlined.

Improved algorithm

The algorithm has been improved to deal with two elastic-plastic bodies in contact. The only change in the previous model is in Eq. 30. Indeed, when the initial geometry is updated, it takes into account the change in both bodies geometry at the same time since h_{ij} is actually the surface separation. At the beginning of each new increment, the pressure is calculated, and this pressure repartition is applied on both counter surfaces. Then, the residual displacement calculated at the end of the increment is added to the initial geometry. If one of the bodies is elastic, then the residual displacement is basically added to the initial geometry, see Fig. 4. Though, if the bodies are both elastic-plastic and have the same hardening behavior, then the surface separation in Eq. 30 becomes:

$$\mathrm{h}_{\mathrm{ij}} \leftarrow \mathrm{h}_{\mathrm{ij}} + 2\mathrm{u}^{\mathrm{r}}_{\mathrm{ij}} \qquad (32)$$

because of the symmetry about the plane of contact, see Fig. 4.

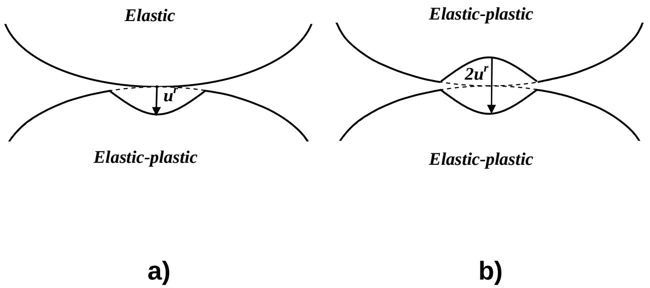

a) b)

Fig. 4 – Updating of the initial geometry with u^r at the beginning of a step. a) Elastic body against elastic-plastic body, b) Contact between 2 elastic-plastic bodies

Results

A simple example is proposed which corresponds to the simulation of the normal contact between two spheres of radius 15 mm. The spheres are made of AISI 52100 bearing steel, with elastic properties *E=210GPa* for the Young modulus, and *ν=0.3* for the Poisson ratio. The hardening law is described by a Swift law, as in Eq. (31), with parameters *B=945MPa*, *C=20*, and *n=0.121*. Here again, e^p is expressed in microdef.

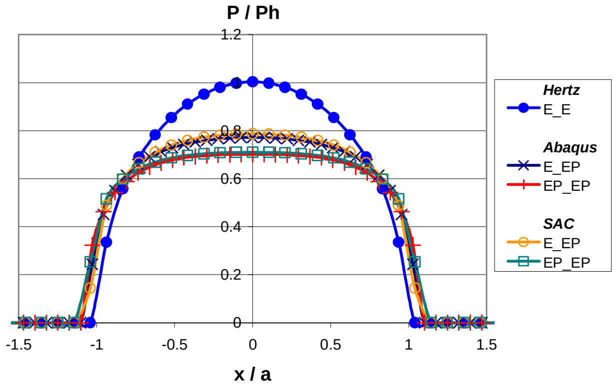

Fig. 5 – Pressure distribution at the end of loading in the plane y=0. Load 11,179N, i.e. P_h=8GPa and hertzian contact radius a=817μm.

In order to compare the results for the loaded case, figure 5 shows the pressure repartition at the end of the loading with a normal load of 11,179N corresponding to a hertzian pressure of 8GPa. The pressure *P* is normalized by the hertzian pressure P_h, and the abscissa *x* by the hertzian contact radius *a*. The axisymmetric FE model consists of 40,247 elements (type CAX4R) with 81,128 dof. Two EP (Elastic-Plastic) situations are presented, the first one with only one inelastic body (E_EP), the second one when both bodies are inelastic (EP_EP, with the same hardening law). As it can be seen, a very good agreement is observed between the results provided by Abaqus and the ones from the Semi-Analytical Code (SAC).

In order to compare the results for the unloaded case, figure 6 shows this time the evolution of the hydrostatic pressure as defined in Eq. 33 versus the depth, in the same conditions as before, i.e. at the end of the loading and with the same hardening law. Again, the hydrostatic pressure is normalized by the hertzian pressure P_h, and the depth *z* by the hertzian contact radius *a*.

$$P_{hydro} = \frac{1}{3}\left(\sigma_1^r + \sigma_2^r + \sigma_3^r\right) \qquad (33)$$

with σ^r_1, σ^r_2, and σ^r_3 the principal components of the residual stress tensor.

As it can be seen again, a very good agreement is observed between the results provided by Abaqus and the ones from the Semi-Analytical Code (SAC).

One may observe two regions where the residual stress state is compressive: at the hertzian depth and at the surface, whereas two tensile regions are found: one between the surface and the hertzian depth, but very close to the surface, and one far below the hertzian depth.

One may also observe that the maximum compressive value is found at depth z/a=0.68, i.e. deeper than the hertzian depth (z/a=0.48).

Almost no variation difference is found in the tensile zones, whereas an important difference in the compressive zone at the hertzian depth is found, the minimum value being smaller when one of the bodies is considered as elastic. For more results concerning the hydrostatic pressure, and the influence of the friction coefficient on its evolution, the reader can refer to [7].

Figure 7 gives the maximum contact pressure and the corresponding maximum equivalent plastic strain versus the normal load at the center of the contact. The dash line indicates the plasticity threshold in term of equivalent plastic strain commonly used to define the yield stress, i.e. $e_p = 0.2\ \%$, that will be used later to define the critical load at the onset of yielding. To find the aforementioned critical value, a polynomial interpolation is used:

$$P^L(x) = \sum_{j=1}^{n} P_j^L(x) \qquad (34)$$

where *x* is equal to 0.2 %, and where P_j^L are the Lagrange polynoms expressed as follows:

$$P_j^L(x) = y_j \prod_{\substack{k=1\\ k\neq j}}^{n} \frac{x-x_k}{x_j-x_k} \qquad (35)$$

where x_j are the values of the equivalent plastic strains, and y_j the values of the loads.

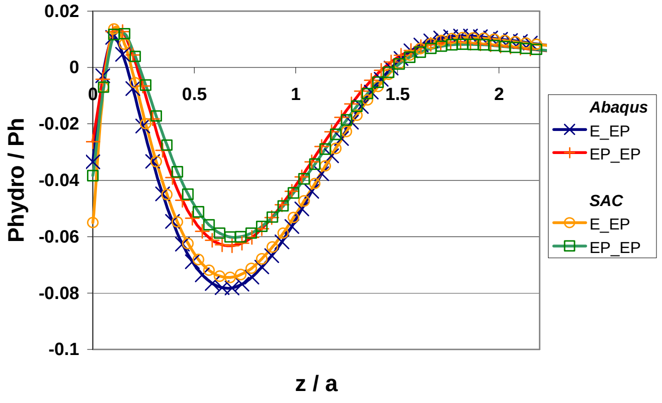

Fig. 6 – Hydrostatic pressure at the end of loading at the center of the contact. Load 11,179N, i.e. P_h=8GPa and hertzian contact radius a=817μm.

One obtains then for the critical loads, *Lc = 1649 N* for the case of the contact between an elastic and an elastic-plastic bodies, and *Lc = 1743 N* for the case of the contact between two elastic-plastic bodies. The latter value will be used in what follows to present now the same results in a dimensionless form, see Fig. 8, the maximum contact pressure *Pmax* being normalized by the Hertz pressure *Ph* and the normal load *L* by the critical load *Lc=1743 N*. An increasing difference between the two curves with increasing load can be seen. As in Fig. 7 one may also observed a pronounced reduction of the maximum contact pressure when considering two EP bodies compared to a purely elastic one against an EP one, up to 11% at the highest load (see Fig. 9). Another interesting trend in Fig. 8 is the discrepancy between the EP response compare to the Hertz solution, at the critical load, i.e. L/Lc=1. Whereas the analysis remains within the classical assumption of elastic behavior, since the plastic strain *ep* does not exceed *0.2%*, it appears that the real contact pressure is 5% lower than the Hertz solution when considering two EP bodies. Note that the difference between the E_EP and the EP_EP solutions is given in Fig. 9 in term of percentage as defined by Eq. 36.

$$C\,(\%) = \frac{\left| P_{\max}^{E\_EP} - P_{\max}^{EP\_EP} \right|}{P_{\max}^{EP\_EP}} \cdot 100 \qquad (36)$$

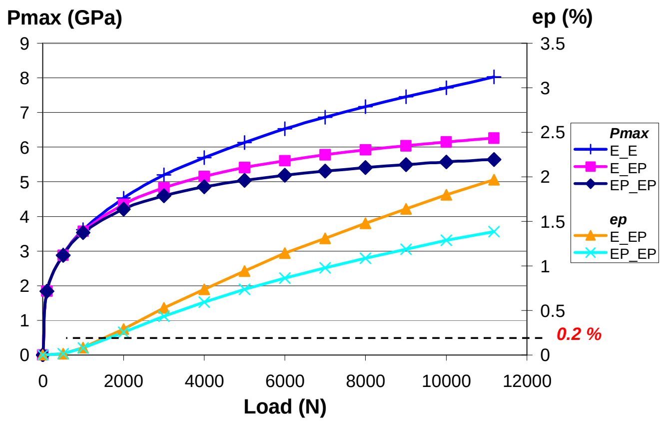

Fig. 7 – Maximum contact pressure P_{max} (GPa) and equivalent plastic strain e^p (%) vs. the normal load (N).

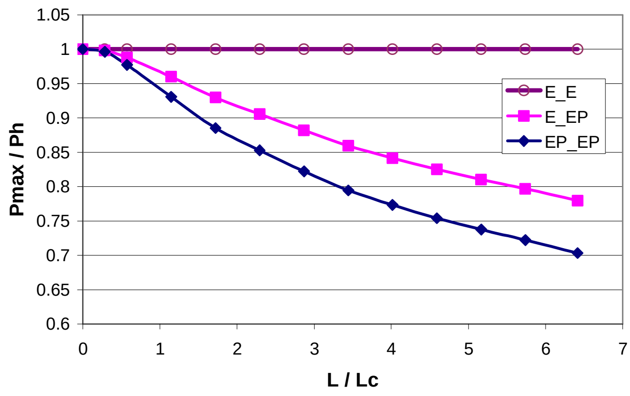

Fig. 8 – Dimensionless contact pressure vs. dimensionless load found at the center of the contact.

From Fig. 9 it can be concluded that for L/L_c < 1, i.e. 4.5GPa for the hertzian pressure, the error made is less than 3%, if only one body behaves inelastically compared to two identical EP bodies in contact. It should be also noticed that, if two different elastic-plastic hardening laws are considered for the bodies in contact, the difference between the E_EP and EP_EP solutions will be lowered, making more appropriate the simplification of considering the harder material as purely elastic.

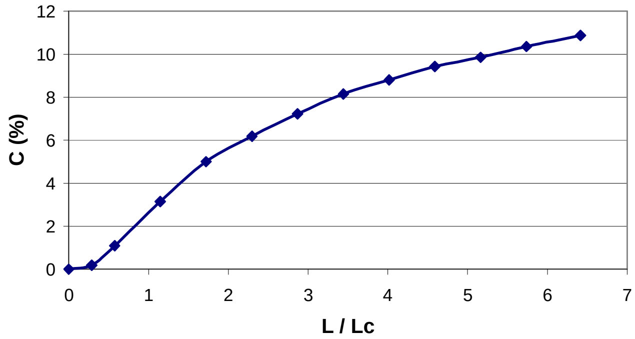

Fig. 9 – Difference between the maximum contact pressures obtained assuming an E_EP and EP_EP behavior vs. the dimensionless load L / L_c

MODELING OF THE ROLLING / SLIDING CONTACT BETWEEN TWO (THERMAL)-ELASTIC-PLASTIC ASPERITIES USING THE DD FORMULATION

This part is considered in a companion paper [17]. In the current incremental procedure, the normal contact is solved at every step. The geometry, the hardening state as well as the plastic strains are updated at the end of each step for each EP body. When the asperities are moving the geometry change includes the permanent deformation of the surface of the elastic-plastic bodies. Special care to the effects of sliding will be given since it is a more complex problem than the pure rolling situation as discussed earlier. Finally, some results on how both the normal and the tangential loads vary during a single tugging will be presented in [17].

CONCLUSION

For modeling an elastic-plastic rolling / sliding contact, a tri-dimensional thermal-elastic-plastic code has been adapted, requiring some specific developments. Two formulations have been proposed to drive the computation, one by imposing the load and the second one by imposing a normal rigid body displacement also call contact interference. Thanks to the use of optimized numerical techniques, which are the Conjugate Gradient and the Discrete Convolution and Fast Fourier Transform, the computation time remains very reasonable in comparison to similar but 2D only analysis performed by FEM, and despite a large number of points in the plastic zone.

The contact between two identical elastic-plastic bodies has been first analyzed. It has been shown a significant reduction of the contact pressure compared to the situation when a purely elastic body is in contact with an elastic-plastic one. In order to complete the study, the tugging between two single asperities is then investigated in a companion paper [17].

REFERENCES

[1] Nogi, T., and Kato, T., 1997, “Influence of a Hard Surface Layer on the Limit of Elastic Contact—Part I: Analysis Using a Real Surface Model,” ASME J. Tribol., **119**, pp. 493–500.

[2] Polonsky, I. A., and Keer, L. M., 1999, “A Numerical Method for Solving Rough Contact Problems Based on the Multi-Level Multi-Summation and Conjugate Gradient Techniques,” Wear, **231**, pp. 206–219.

[3] Lubrecht, A. A., and Ioannides, E., 1991, “A Fast Solution of the Dry Contact Problem and the Associated Sub-Surface Stress Field, Using Multilevel Techniques,” ASME J. Tribol., **113**, pp. 128–133.

[4] Liu, S., Wang, Q., and Liu, G., 2000, “A Versatile Method of Discrete Convolution and FFT (DC-FFT) for Contact Analyses,” Wear, **243**, pp. 101–111.

[5] Jacq, C., Nélias, D., Lormand, G., and Girodin, D., 2002, “Development of a Three-Dimensional Semi-Analytical Elastic–Plastic Contact Code,” ASME J. Tribol., **124**, pp. 653–667.

[6] Boucly, V., Nélias, D., Liu, S., Wang, Q. J., and Keer, L. M., 2005, “Contact Analyses for Bodies With Frictional Heating and Plastic Behavior,” ASME J. Tribol., **127**, pp. 355–364.

[7] Nélias, D., Antaluca, E., Boucly, V., and Cretu, S., 2006, “A 3D Semi-Analytical Model for Elastic-Plastic Sliding Contacts,” submitted.

[8] Jacq, C., Lormand, G., Nélias, D., Girodin, D., and Vincent, A., 2003, “On the Influence of Residual Stresses in Determining the Micro-Yield Stress Profile in a Nitrided Steel by Nano-Indentation,” Materials Science and Engineering A, **342**, pp. 311-319.

[9] Sainsot, P., Jacq, C., and Nélias, D., 2002, “A Numerical Model for Elastoplastic Rough Contact,” Computer Modeling in Engineering & Sciences, **3** (4), pp.497-506.

[10] Gallego, L., Nélias, D., and Jacq, C., 2006, “A Comprehensive Method to Predict Wear and to Define the Optimum Geometry of Fretting Surfaces,” ASME J. Tribol., **128**, pp. 476-485.

[11] Nélias, D., Boucly, V., and Brunet, M., 2006, “Elastic-Plastic Contact Between Rough Surfaces: Proposal for a Wear or Running-in Model,” ASME J. Tribol., **128**, pp. 236–244.

[12] Liu, S., and Wang, Q., 2001, “A Three-Dimensional Thermomechanical Model of Contact Between Nonconforming Rough Surfaces,” ASME J. Tribol., **123**, pp. 17–26.

[13] Johnson, K. L., *Contact Mechanics*, Cambridge Univ. Press, Cambridge, 1985, Chaps. 3, 4.

[14] Green, I., 2005, “Poisson Ration Effects and Critical Values in Spherical and Cylindrical Hertzian Contacts,” Int. J. Appl. Mech. And Eng., **10**(3), pp. 451-462.

[15] Fotiu, P. A., and Nemat-Nasser, S., 1996, “A Universal Integration Algorithm for Rate-Dependant Elastoplasticity,” Comput. Struct., **59**, pp. 1173-1184.

[16] El Ghazal, H., 1999, “Etude des propriétés microstructurales et mécaniques des aciers 16NiCrMo13 cémenté et 32CrMoV13 nitruré-Application à la prévision de leur limite d’endurance en fatigue de roulement,” Ph.D. Thesis, INSA Lyon, France.

[17] Boucly, V., Nélias, D., and Green, I., 2006, “Modeling of the Rolling and Sliding Contact Between two Asperities. Part II: Hemispherical Sliding Contact,” Proc. of IJTC2006, STLE-ASME Int. Joint Trib. Conf., October 22-25, 2006, San Antonio, TX, USA, Paper IJTC2006-12274.